







RESEARCH ARTICLE | OCTOBER 19 2023

Light-guiding-light-based temporal integration of broadband terahertz pulses in air

Jiayu Zhao ; Feifan Zhu ; Yongpeng Han ; Qining Wang ; Li Lao; Xiaofeng Li; Yan Peng ; Yiming Zhu 

 Check for updates

APL Photonics 8, 106107 (2023)
<https://doi.org/10.1063/5.0158107>



View Online



Export Citation

CrossMark

Articles You May Be Interested In

A functional integral formalism for quantum spin systems


J. Math. Phys. (July 2008)

Modes selection in polymer mixtures undergoing phase separation by photochemical reactions

Chaos (June 1999)

Spreading of a surfactant monolayer on a thin liquid film: Onset and evolution of digitated structures


Chaos (March 1999)



yttrium iron garnet, zeolites, nano ribbons, epitaxial crystal growth, cerium oxide polishing powder, surface functionalized nanoparticles, sapphire windows, Nd:YAG, spintronics, raman substrates, silver nanoparticles, perovskites, MOCVD, beta-barium borate, rare earth metals, quantum dots, osmium, scintillation Ce:YAG, refractory metals, laser crystals, anodic aluminum oxide, niobate, InAs wafers, MOFs, AuNPs, ZnS, CdTe, perovskite crystals, transparent ceramics

glassy carbon, III-IV semiconductors, barium fluoride, ultra high purity materials, europium phosphors, photonics, infrared dyes, transparent ceramics, CIGS, cermet, nanodispersions, MBE grade materials, thin film, OLED lighting, solar energy, sputtering targets, fiber optics, h-BN, deposition slugs, CVD precursors, photovoltaics, metamaterials, borosilicate glass, YBCO, superconductors, InGaAs, indium tin oxide, MgF2, rutile, optical glass, diamond micropowder

beamsplitters, fused quartz, additive manufacturing, organometallics, copper nanoparticles, gallium lump, transparent ceramics, CIGS, cermet, nanodispersions, MBE grade materials, thin film, OLED lighting, solar energy, sputtering targets, fiber optics, h-BN, deposition slugs, CVD precursors, photovoltaics, metamaterials, borosilicate glass, YBCO, superconductors, InGaAs, indium tin oxide, MgF2, rutile, optical glass, diamond micropowder



Now Invent.™

www.americanelements.com

© 2001-2022, American Elements LLC, a U.S. Registered Trademark

The Next Generation of Material Science Catalogs

Light-guiding-light-based temporal integration of broadband terahertz pulses in air

Cite as: APL Photon. 8, 106107 (2023); doi: 10.1063/5.0158107

Submitted: 15 May 2023 • Accepted: 3 October 2023 •

Published Online: 19 October 2023



View Online



Export Citation



CrossMark

Jiayu Zhao,^{1,2,a)}  Feifan Zhu,¹  Yongpeng Han,¹  Qining Wang,¹  Li Lao,³ Xiaofeng Li,¹ Yan Peng,^{1,2,a)} 
and Yiming Zhu^{1,2,a)} 

AFFILIATIONS

¹Terahertz Technology Innovation Research Institute, Terahertz Spectrum and Imaging Technology Cooperative Innovation Center, Shanghai Key Lab of Modern Optical System, University of Shanghai for Science and Technology, Shanghai 200093, China

²Shanghai Institute of Intelligent Science and Technology, Tongji University, Shanghai 200092, China

³Tera Aurora Electro-optics Technology Co., Ltd., Shanghai 200093, China

^{a)}Authors to whom correspondence should be addressed: zhaojiayu@usst.edu.cn, py@usst.edu.cn and ymzhu@usst.edu.cn

ABSTRACT

The next generation of all-optical computation platforms prefers the light-guiding-light (LGL) scheme inside a medium that envisions circuitry-free and rapidly reconfigurable systems powered by dynamic interactions between light beams. Currently, suitable LGL materials and corresponding mechanisms are in urgent need. In this work, we proposed ubiquitous air as a restorable LGL signal manipulation medium with transient air-plasma waveguide circuits. Briefly, by focusing femtosecond laser beams in free space, the created atmospheric plasma filament array via photoionization was able to guide terahertz (THz) pulses along its epsilon-near-zero zone with a $1/f$ -profile spectral response. Consequently, this achieved a time-domain integration of the THz pulse in broad bandwidth. When the pumping laser was sequentially turned off and on, this air-plasma multi-filament structure was erased and rebuilt within nano- and femto-seconds, respectively, allowing rapid and repeated rearrangements of the all-optical stage. Furthermore, this air-based LGL information processing approach is promising to pave the way toward all-optical calculations during free-space directional transmission of THz waves, in which way the delivered THz signal can be remotely controlled.

© 2023 Author(s). All article content, except where otherwise noted, is licensed under a Creative Commons Attribution (CC BY) license (<http://creativecommons.org/licenses/by/4.0/>). <https://doi.org/10.1063/5.0158107>

I. INTRODUCTION

All-optical computations, which overcome the speed limitation imposed by photoelectric-based systems, are done solely with light beams guided in solid circuits composed of silicon-substrate channels,^{1,2} metal wires,^{3,4} optical fibers,⁵ etc. Meanwhile, solid and gas hybrid media have also been frequently employed,^{6–10} in which case, although light could propagate in air (free space or air trenches), it necessitates support from hardware, including epsilon-near-zero (ENZ) substrates, phase masks, digital micromirror devices, etc. Hence, these computational systems are still built on solid bases. Recently, the next generation of light-guiding-light (LGL) schemes inside liquid-solid phase-transition photonic media has attracted intense attention in the community, which envisions

circuitry-free, reconfigurable, and multilayered computing setups powered by dynamic interactions between light beams.¹¹ Reversible soft hosts, e.g., photoresponsive gels¹¹ and photopolymers,¹² have been proposed for LGL signal processing in order to remove those rigid circuit components. However, these processes continue with the participation of quasi-solid media. By contrast, there are few reports on all-optical computing being performed entirely without the assistance of solid materials, not to mention being solely in gases.

Actually, besides these solid platforms, the gaseous substance (air) can also be a potential candidate for the LGL material, which features a unique free-space location of performance. For instance, when focusing femtosecond laser beams in air, the atmospheric plasma filament array is created via photoionization,^{13,14} which can

further guide the propagation of terahertz (THz) waves,¹⁵ hence realizing the LGL effect with air as the only medium. Moreover, this gas-based stage can be rapidly restorable since the lifetime of air plasma is within nanoseconds,¹⁴ which means that once the driven laser is turned off, plasma ions and electrons recombine immediately, and then the ambient air returns to its original state, allowing repeated reconfiguration of the plasma waveguides. Additionally, considering the thermal effect induced by the high laser repetition frequency,^{16–18} the air restoration time is still on the order of milliseconds. This value is advantageous compared with publications in the same LGL-based scheme for all-optical calculations, where it could take, e.g., several to tens of seconds for the gels¹¹ to recover from the photo-induced modification, and then the gels can be exposed to light again for reshaping new computational circuits inside.

Yet for now, although the establishment of a plasma array inside the air is routine,^{19–21} the underlying mechanism of THz field guidance along one single laser filament region is still not comprehensively understood, which further forms the obstacle to implement interactions between multiple THz channels. For this reason, building blocks of the air-plasma THz computing circuit with basic functionalities (like calculus) remain absent and challenging. Fortunately, recently, the epsilon-near-zero (ENZ, $\text{Re}[\epsilon_r] \sim 0$) effect of the air plasma filament in the THz band was revealed²² to interpret the strong near-field confinement of THz amplitude during laser filamentation. This has opened the pathway to designing fundamental plasma devices for all-optical THz signal processing in the air.

In this work, we first numerically built a double-filament array with a THz-ENZ zone generated inside the filaments' gap. Then, we varied the sub-millimeter separation between the parallel plasma columns in order to optimize the spatial confinement and guidance of THz waves along this ENZ channel. Accordingly, the spectral transfer function was achieved in a $1/f$ shape (f : THz frequency), which in the principle of mathematics, gives birth to a temporal integration of the input THz signal in broad bandwidth (Secs. II and III). One schematic diagram of this all-optical computing stage is displayed in Fig. 1(a), where a single-cycle THz pulse in the time domain (E_{in}) is integrated in the form of $E_{out} = \int E_{in} dt$ via the designed dual-filament circuitry. This air-based LGL calculation represents a novel innovation as it completely gets rid of the (quasi-)solid materials mentioned above. At last, the above theoretical expectations have been experimentally confirmed in Secs. IV–VII with both two- and four-filament arrays. Furthermore, this free-space laser-guiding-THz signal manipulation is promising to validate all-optical computing during remotely directional transmission of THz waves in the air,²³ which means the delivered THz information could be processed by remote control.

II. THE ENZ ZONE OF AIR-PLASMA STRUCTURES WITH THE THz INTEGRATION FUNCTIONALITY

In the principle of mathematics as demonstrated in supplementary material S1, for an ideal time integration device whose output temporal signal (E_{out}) is the first-order time integration of the input E_{in} , the ratio of spectral signals satisfies the $1/f$ relation as

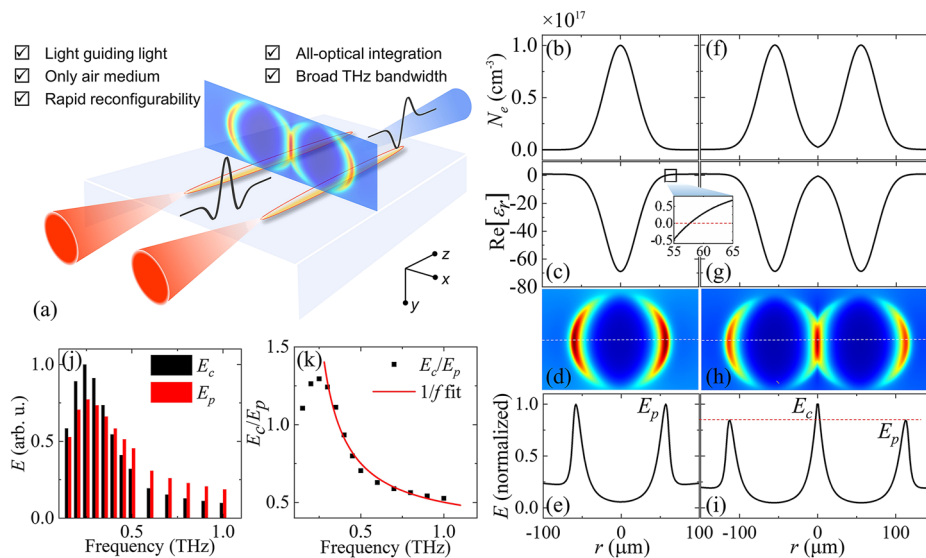


FIG. 1. (a) The concept of all-optical THz integration via the air-plasma platform, which consists of two identical parallel laser filaments separated by a sub-millimeter gap. The transverse picture in the x - y plane indicates the confined THz mode field mainly inside the double filaments' gap. For a single plasma filament: (b) the radial distribution of plasma density (N_e), (c) the real part of the dielectric constant ($\text{Re}[\epsilon_r]$), and (d) the simulated electric field distribution of the confined THz mode at 0.3 THz with (e) its radial profile along the x axis. (f)–(i) Corresponding results in the case of the parallel double-filament array. (j) The central THz electric field (E_c , black bars), the peripheral one (E_p , red bars), and (k) the calculated E_c/E_p as a function of the THz frequency (squares) and the corresponding $1/f$ fitting curve (red line).

$$\frac{\mathcal{F}[E_{out}]}{\mathcal{F}[E_{in}]} \propto \frac{1}{if}, \tag{1}$$

where i is the imaginary unit. This mathematical relationship can be experimentally realized by near-field light confinement approaches.^{3,24,25} Briefly, inside a near-field spatial region, the input lower- f component (with a larger wavelength) was more tightly constrained into a stronger mode-field outcome, which resulted in the desired $1/f$ -shape spectral response. In this direction, the ENZ effect is also well-known for its mode field squeezing capability in narrow channels.^{26,27} Besides, we recently found that the laser plasma filament could serve as an ENZ carrier of THz waves.²² Therefore, it is natural for us to consider the possibility of ENZ-plasma-based THz integration.

In order to investigate the ENZ region of the plasma filament as well as interactions between ENZ channels for potential all-optical THz integration, we carried out numerical simulations of the constrained THz mode within the air-plasma area. First, in the case of a single laser filament, it could be simplified as a plasma column with a radial free-electron-density distribution (N_e) determined by a two-dimensional Gaussian function as

$$N_e = N_{e0} \exp\left(-\frac{x^2 + y^2}{b^2}\right), \tag{2}$$

where N_{e0} denotes the central plasma density set at $1.0 \times 10^{17} \text{ cm}^{-3}$, and $b = 30 \text{ }\mu\text{m}$ is the half width at $1/e$ of the plasma column, whose full width at half maximum (FWHM) is about $50 \text{ }\mu\text{m}$. The radial distribution of N_e is plotted in Fig. 1(b), according to which the relative dielectric constant ϵ_r is calculated by

$$\epsilon_r = 1 - \frac{\omega_p^2}{\omega^2 - if_c\omega}, \tag{3}$$

where ω is the THz angular frequency, and ω_p indicates the plasma frequency given by

$$\omega_p = \sqrt{\frac{e^2}{m_e\epsilon_0}N_e}, \tag{4}$$

where e represents the electric charge, m_e indicates the effective mass of the electron, and ϵ_0 is the permittivity in vacuum. $f_c \sim 1 \text{ THz}$ corresponds to the typical electron collision frequency inside the filament.²⁸ Figure 1(c) displays the radial distribution of $\text{Re}[\epsilon_r]$ at $f = 0.3 \text{ THz}$ inside the plasma filament, which increases toward the filament periphery and approaches unity. In addition, there is a positive-negative dielectric interface ($\text{Re}[\epsilon_r] = 0$) near the filament periphery at approximately $r = 58 \text{ }\mu\text{m}$ (see inset).

Based on this $\text{Re}[\epsilon_r]$ evolution, numerical simulations were carried out by the COMSOL software, and the simulated mode field at $f = 0.3 \text{ THz}$ is shown in Fig. 1(d). Then, the radial electric field distribution E along the x axis was taken out and shown in Fig. 1(e). In view of Figs. 1(d) and 1(e), E has been spatially limited close to the filament periphery where $\text{Re}[\epsilon_r] = 0$ instead of the filament center. This result agrees with the 1DND analytical model as indicated in supplementary material S2.

Next, in order to further enhance the THz wave confinement, similar simulations were also performed for the case of parallel

plasma filaments separated by a distance of $2d \sim 100 \text{ }\mu\text{m}$. The N_e distribution of the double filaments is determined by

$$N_e = N_{e0} \exp\left\{-\frac{[x - d \cdot \text{sgn}(x)]^2 + y^2}{b^2}\right\}, \tag{5}$$

where the filaments' centers are along the x axis and $\text{sgn}(x)$ denotes the sign of x . Corresponding radial distributions of N_e and $\text{Re}[\epsilon_r]$ are plotted in Figs. 1(f) and 1(g), respectively. Similar to the single filament case, there is $\text{Re}[\epsilon_r] = 0$ at the filament periphery. Moreover, in the gap area of the double filaments, $\text{Re}[\epsilon_r]$ also approached zero, together with dramatic decreases toward the two filaments' centers. This unique $\text{Re}[\epsilon_r]$ distribution has led to such a simulated result, as shown in Fig. 1(h). A tighter confinement of the THz mode field inside the filaments' gap has been induced by the synthesis of two THz-ENZ channels. This point is further highlighted in Fig. 1(i) with E along the x axis, where the central THz electric field (E_c) contributed by both filaments is stronger than the peripheral one (E_p) formed by one single filament.

Following Eq. (1), the next concern is the frequency dependence of E_c/E_p . This issue was clarified by repeating simulations within 0.1 to 1 THz (supplementary material S3). The resultant E_c and E_p are shown in Fig. 1(j), both of which first increase and subsequently decrease. It can also be seen that E_p is less than E_c in the low THz band but increases to exceed E_c after 0.4 THz. Finally, the calculated E_c/E_p are shown in Fig. 1(k) as black squares, which mainly indicate a decreasing spectral response as a function of THz frequency as expected from the near-field confinement effect.^{3,25} Remarkably, this result can be fitted by a $1/f$ curve, i.e.,

$$\left|\frac{E_c(f)}{E_p(f)}\right| \propto \frac{1}{f}, \tag{6}$$

as shown as the red line in Fig. 1(k). Since Eq. (6) meets the mathematical expectation of Eq. (1), it is promising to perform time integration of broadband THz signals by the ENZ-based air filament array. It is also noticed that ENZ materials or the air trenches therein were used to perform optical computing.^{6,7,29,30} However, the computational mechanisms in these works are different from ours. For example, ITO²⁹ underwent changes in its intrinsic properties (like the permittivity and the absorption coefficient) upon interaction with the incident laser, so the output laser power manifested bistability, which enabled rapid and dependable all-optical binary behavior. Another example⁷ is the application of reprogrammable ITO nanoelements inside air trenches for interaction with the confined light, which can solve partial differential equations (PDEs) by tuning the optical properties of the nanoelements. Recently, ENZ metamaterials with designed transmission functions were also employed to perform calculus on input signals,³¹ while their electronic circuits and mechanisms are still applied for the single frequency point instead of our all-optical method in broad bandwidth.

III. OPTIMIZATION OF CONFIGURATION PARAMETERS FOR THE FILAMENTS ARRAY

To optimize this laser-guiding-THz interaction, the air separation ($2d$) between the plasma columns was varied from 90 to 125 μm during simulations (supplementary material S4). Meanwhile, E_c and

E_p were extracted and shown in Fig. 2(a), inside which E_c peaked at around $2d = 110 \mu\text{m}$ while E_p slightly decreased with respect to $2d$. Furthermore, we also calculated E_c/E_p , as shown in Fig. 2(b), which was used to evaluate the enhancement factor of spatial THz confinement by the double-filament array compared with the single one. One can see that the range for E_c/E_p above unity (dotted red line) appeared at around $2d = 110 \mu\text{m}$. Therefore, this $2d$ result was adopted in our following simulations and experiments. It is also worth mentioning that our case differs from two metal wires,³ which always preferred a smaller $2d$ in order to achieve stronger THz confinement and an improved integration effect with reduced errors. This issue has been studied as follows.

By calculating $\text{Re}[\varepsilon_r]$ as $2d$ decreased from 125 to 90 μm as shown in Figs. 2(c) and 2(d), it can be seen that the FWHM of the central gap (double-headed arrow) reduced with respect to the decreasing $2d$, which would in principle induce a tighter THz mode field confinement inside the gap like that in Ref. 3. However, at the same time, the $\text{Re}[\varepsilon_r]$ value in the gap varied significantly, which also needs to be considered. (i) For $2d$ in the range from 125 to 110 μm , $\text{Re}[\varepsilon_r]$ at $r = 0$ is around zero (ENZ point), as shown detailedly in Fig. 2(d), and the plasma gap is capable of well confining the THz field. (ii) Nevertheless, when $2d$ decreased toward 90 μm , $\text{Re}[\varepsilon_r]$ is much smaller than zero, and the ENZ effect is no longer valid. Therefore, the confined THz field inside the filaments' gap is a balance between $2d$ and the central $\text{Re}[\varepsilon_r]$ values. Hence, the maximum THz field has been obtained at approximately $2d = 110 \mu\text{m}$ rather than at a lower $2d$. The above conclusions regarding the effect of dual-filament distance on the THz confinement differ from those of Ref. 3. This is mainly due to the Gaussian N_e distribution of the plasma filament, which is distinct from the step-like N_e distribution of metallic wires. Therefore, the variation of the filaments' distance inevitably changes both the gap width and the ENZ condition at the

center. Apart from this, the effect of filament diameter variation is another point of difference from Ref. 3. Please see supplementary material S5.

We also calculated the radial $\text{Re}[\varepsilon_r]$ with a varying N_e (0.2×10^{17} – $2.0 \times 10^{17} \text{ cm}^{-3}$) at $f = 0.3 \text{ THz}$ and $2d = 110 \mu\text{m}$ by Eqs. (3)–(5), and showed the results in Fig. 2(e). It can be observed that two $\text{Re}[\varepsilon_r]$ dips became deeper with increasing N_e (along the vertical arrow). Based on these $\text{Re}[\varepsilon_r]$ profiles in Fig. 2(e), COMSOL simulation outcomes of E_c/E_p are shown in Fig. 2(f), which increased with the increasing N_e (supplementary material S6). Since this enhanced E_c/E_p represented a tighter THz confinement inside the filaments' gap as well as a stronger integration effect, it can be concluded that the THz integration became more valid with the increasing N_e .

IV. DESIGN OF THE EXPERIMENTAL SETUP

To experimentally confirm the above points, a laser-pumping THz time-domain spectroscopy system³² was established (Fig. 3) for both generation of the filament array and acquisition of the output THz signal. Specifically, Ti:sapphire laser pulses in repetition rate of 1 kHz, central wavelength of 800 nm, duration of 100 fs and energy of 2 mJ/pulse were split into two paths as the pump beam (~1.8 mJ/pulse) and the probe, respectively. Especially for the pumping beam, it was focused by a lens with a focal length of 30 cm, before which a beam compressor and a semicircular phase plate¹⁹ were also inserted into the beam path for the following three reasons:

- (1) In view of the simulation results in Sec. III, the separation $2d$ between two filaments should be down to ~110 μm to maintain $E_c/E_p > 1$, i.e., the integration effect. However, this

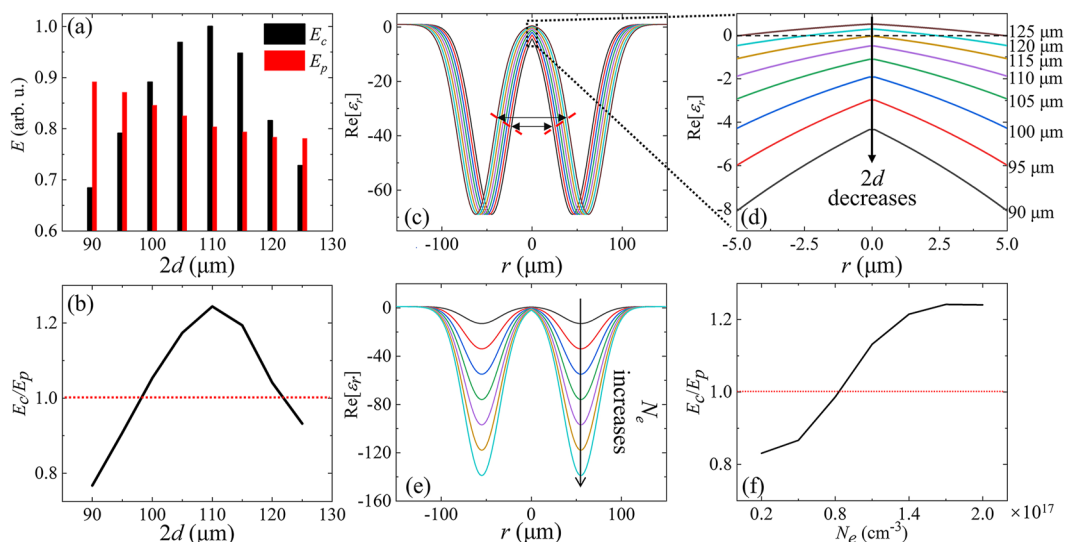


FIG. 2. (a) The central THz electric field (E_c , black bars), the peripheral one (E_p , red bars), and (b) the calculated E_c/E_p as a function of the distance $2d$ between two filaments. The calculated $\text{Re}[\varepsilon_r]$ distributions in the radial direction as a function of $2d$ (c) and (d), and N_e (e). From top to bottom, N_e varied from 0.2×10^{17} to $2.0 \times 10^{17} \text{ cm}^{-3}$. (f) The simulated E_c/E_p as a function of N_e according to the COMSOL model established upon (e).

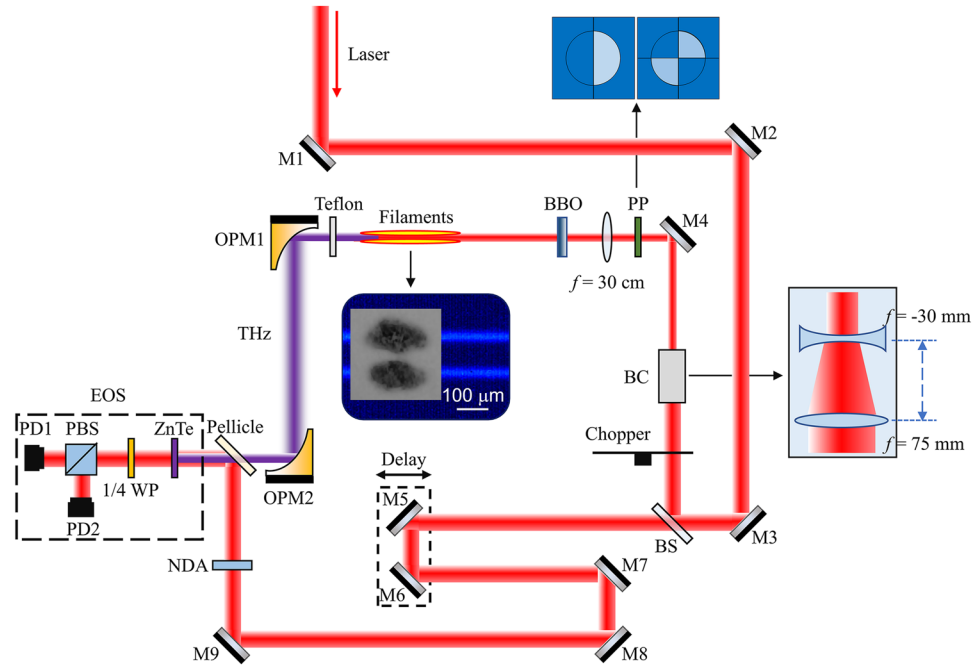


FIG. 3. The experimental setup. Around the geometric focus of the lens, a 20-mm-length parallel double-filament array was created with a separation distance of about $115 \mu\text{m}$. Inset: the side image of the generated two filaments and the burning pattern on the thermal paper by inserting it transversely into the two-filament array. M: mirror. BS: beam splitter. BC: beam compressor. PP: phase plate. OPM: off-axis parabolic mirror. NDA: neutral density attenuator. WP: wave plate. PBS: polarization beam splitter. PD: photodiode. EOS: electro-optic sampling.

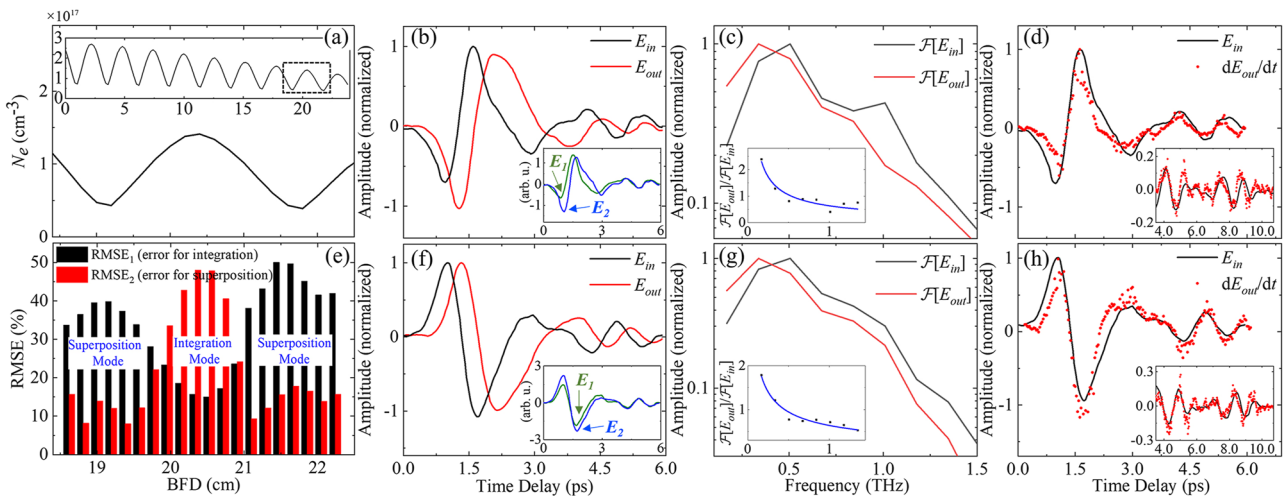


FIG. 4. While BFD (BBO-to-focus distance) was varied, (a) the calculated N_e given by the photocurrent model and (e) the calculated RMSE_1 for errors of the integration effect (black bars) and RMSE_2 for errors of the superposition effect (red bars). (b) At BFD = 20.5 cm, the THz waveform from the double-filament array (red line, as E_{out}) and the average THz signal (black line, as E_{in}) achieved from E_1 and E_2 of each single filament (inset). (c) THz spectra of E_{in} (black line, as $\mathcal{F}[E_{in}]$) and E_{out} (red line, as $\mathcal{F}[E_{out}]$) obtained by Fourier transforms on signals in (b). Inset: $\mathcal{F}[E_{out}]/\mathcal{F}[E_{in}]$ (black squares) and its $1/f$ -fitted curve (blue line). (d) E_{in} (black line) and the first-order time derivative of E_{out} (i.e., dE_{out}/dt , red circles). Inset: oscillations of the THz waveform after the main pulse in repeated tests. (f)–(h) THz signals recorded in the case of the BBO crystal being moved toward the laser focus by a ω - 2ω dephasing length.

20 October 2023 02:12:25

value is almost the diameter of one single filament, and at such a close distance, the two filaments are just about to be separated according to Ref. 33. Hence, optical alignment is critical, and normally, the separation between two filaments could be achieved at $150\ \mu\text{m}$ ³⁴ in traditional schemes like independent control of each filament. In order to further decrease $2d$ while avoiding filament fusion, in this work we adopted a phase plate, which is divided into two parts with π phase lag at $800\ \text{nm}$,¹⁹ to create the desired double filament array. Since there is always a laser destructive interference area between the two parts of the phase plate, the filaments' fusion is prevented.

- (2) Moreover, according to the theory in Ref. 19, the separation distance between filaments is mainly determined by the focal length of the focusing lens, which should be shorter than $50\ \text{cm}$ if $2d = 110\ \mu\text{m}$ is the target. In our tests, the focal length of $30\ \text{cm}$ was finally employed, and the detected $2d$ was about $115\ \mu\text{m}$. This can be seen from the resultant two filaments in the inset of Fig. 3, which were captured by both the thermal paper and the side image methods.
- (3) In addition, remind ourselves that the simulated $1/f$ spectral response, as shown in Fig. 1(k), is in ideal conditions that assume an infinite filament length. Therefore, in actual experiments, a large filament length is required to ensure the accumulation of the integration effect. In this aspect, it was found that although the growth of the pumping laser energy could extend the filament length, it also brought an increase in filament separation. By contrast, a beam compressor of the laser spot size (from 13 to $5\ \text{mm}$) has been used by us to elongate the filament from about 6 to $20\ \text{mm}$ at the same time with little impact on the filaments' separation.

Therefore, the final experimental setup is shown in Fig. 3. Besides, a 0.1-mm -thick Type-I β -barium borate (BBO) frequency-doubling crystal was used to modulate the plasma density of the filaments by varying the BBO to focus distance (BFD). At this moment, the relative phase difference between the fundamental laser (ω) and its second harmonic (2ω) periodically oscillated between 0 and 2π , thus changing the N_e value (see Fig. 4). The THz signal after the filaments was filtered by a Teflon plate for separation from the pumping laser and eventually detected by the probe beam in a standard EOS (electric-optic sampling) setup.³² The employed ZnTe crystals were (110)-oriented in thickness of $1.5\ \text{mm}$ for 1.5-THz -bandwidth detection (in Secs. V and VI) and $0.5\ \text{mm}$ for 3-THz -bandwidth detection (in Sec. VII), respectively.

V. TIME-DOMAIN THz INTEGRATION INSIDE THE DUAL-FILAMENT ARRAY

As shown in the inset of Fig. 4(a) (see also supplementary material S7 for more modal calculations), N_e as a function of BFD has been calculated according to the static tunneling ionization method within the photocurrent model.^{35–37} The dashed box is enlarged and displayed in the same figure. It can be seen that a maximum N_e of about $1.4 \times 10^{17}\ \text{cm}^{-3}$ appeared at around BFD = $20.5\ \text{cm}$, where the THz integration effect should take place according to Fig. 2(f). For the minimum N_e points, the integration effect might not be well observed. This point has been proved

by setting BFD at $20.5\ \text{cm}$ as an example and investigating the corresponding integration effect.

It is worth noting that, besides the filament array playing the role of THz-ENZ waveguides, each of the plasma filaments radiated THz waves by itself, which can be retrieved by simply blocking one-half of the phase plate and passing the pumping laser through the other half. Under this condition, two filaments were created alternately, and the emitted THz waveforms (E_1 and E_2) were recorded, respectively, as shown in the inset of Fig. 4(b), where E_1 and E_2 were both single-cycle temporal THz pulses with similar profiles (see corresponding spectra in supplementary material S8). Moreover, the plasma could be produced within the same temporal scale as the pumping laser pulse duration,³⁵ i.e., $\sim 100\ \text{fs}$, while the plasma's average lifetime is as long as several nanoseconds.^{13,14} In contrast, the THz pulse induced by the residual current following the laser pulse³⁵ has a duration of a few picoseconds, much longer than the creation of plasma but much shorter than the plasma's lifetime. This fact hints that the plasma could be formed in an instant before the THz pulse. Afterward, it would last enough time for interaction with the THz wave. Therefore, the air-plasma filament array enables a THz transmission effect^{15,38,39} and can be treated as a static THz waveguide, along which E_1 and E_2 were both confined inside the central ENZ zone, as simulated in Fig. 1. Arising from this actuality, the output THz signal (E_{out}) after the double-filament array is expected to be in the form of $E_{out} = \int E_{in} dt$, where E_{in} is contributed by E_1 and E_2 . Since E_1 and E_2 have similar profiles, we adopted their average waveform in normalized form as E_{in} of this all-optical system, as displayed in Fig. 4(b) as the black line. On the other hand, E_{out} was detected with the whole filament array, as shown in Fig. 4(b) as the red line (also normalized). It is noticed that waveforms in Fig. 4 are mostly normalized for analyses, which is reasonable because, for the temporal signal and its calculus signal, the waveform profile matching is the central concern, while quantitative comparisons are meaningless.

The normalized spectra of E_{in} and E_{out} via Fourier transforms are presented in Fig. 4(c), which shows a considerable low-frequency enhancement and high-frequency attenuation of $\mathcal{F}[E_{out}]$ with respect to $\mathcal{F}[E_{in}]$. The inset of Fig. 4(c) depicts the ratio between $\mathcal{F}[E_{out}]$ and $\mathcal{F}[E_{in}]$, which unveils an essential match with the $1/f$ response associated with a time integrator as defined in Eqs. (1) and (6). Besides, the spectral phase difference also follows the integration principle, which can be seen in supplementary material S9. To finally confirm this integration functionality, we calculated the first-order time derivative of E_{out} (i.e., dE_{out}/dt) and compared it with the E_{in} waveform rather than integrating E_{in} to match E_{out} . This strategy has the advantage of minimizing the effects of numerical artifacts, which could lead to alterations of the THz pulse shape (see detailed information in supplementary material S10). The calculated dE_{out}/dt together with E_{in} are shown in Fig. 4(d), with an agreement on the pulse profiles. The inset of Fig. 4(d) further proves this point with signal oscillations following the main THz pulse in repetitive tests. Therefore, the capability of time-domain integration has been demonstrated by the parallel air-filament array in the THz band.

Next, the root mean squared error $\text{RMSE}(x_i, X_i)$ = $\sqrt{\frac{1}{n} \sum_{i=1}^n (x_i - X_i)^2}$ was used to quantitatively estimate the matching degree between E_{in} (average waveform of E_1 and E_2 , and normalized) and dE_{out}/dt (normalized)—as RMSE_1 . Here, n is the number of THz waveform samples, x_i is each sample value of

E_{in} , and X_i is that of dE_{out}/dt . The calculated $RMSE_1$ for Fig. 4(d) is about 15% at $BFD = 20.5$ cm. By repeating experiments with other BBO locations, all $RMSE_1$ values were shown in Fig. 4(e) as black bars as a function of BFD. Specifically, $RMSE_1$ achieved larger values when BFD deviated from 20.5 cm. By visiting the correlation between Figs. 4(a) and 4(e), we noticed that $RMSE_1$ is actually inversely proportional to the N_e value. This phenomenon can be attributed to Fig. 2(f), which shows that the proposed THz integration effect could be strengthened (with a smaller $RMSE_1$) by increasing N_e . Furthermore, we noticed that E_c/E_p started to be above 1 at about $N_e = 0.8 \times 10^{17} \text{ cm}^{-3}$ and tended to be saturated at $N_e = 1.7 \times 10^{17} \text{ cm}^{-3}$, as shown in Fig. 2(f). This phenomenon hints that the spatial confinement of THz energy between the double plasma filaments, as well as the following THz integration effect, can be significantly changed when N_e just varies around twice. In addition, the N_e maximum ($\sim 1.4 \times 10^{17} \text{ cm}^{-3}$) in Fig. 4(a) was more than three times larger than the minimum ($\sim 0.4 \times 10^{17} \text{ cm}^{-3}$). Therefore, this N_e variation range is able to give rise to the appearance or disappearance of the synthetic THz mode in the gap and the integration phenomenon.

On the other hand, when N_e was too weak to support this gap mode, the two filaments had no more interactions with each other. At this moment, the integration effect would be overtaken by the alternative THz superposition^{34,40} of two independent filaments. This can also be seen in Fig. 4(e) from the red bars ($RMSE_2$), which were calculated by the RMSE formula between E_{in} ($=E_1 + E_2$, non-normalized) and E_{out} (non-normalized) with respect to BFD. One can see that at $BFD = 20.5$ cm, the THz integration mode dominated ($RMSE_1 < RMSE_2$). However, when there was a deviation from this BFD value and N_e decreased, $RMSE_1$ rapidly increased with the decrease in $RMSE_2$. Hence, on this occasion, the original integration mode was converted into the coherent addition pattern, which took the leading role. Anyway, the THz integration effect can always be found with the modulated N_e maximum by moving the BBO location of the air-plasma platform. In consideration of the above analyses, we additionally checked the THz signals at another N_e maximum with the BBO position moved toward the laser focus by a $\omega-2\omega$ dephasing length⁴¹ ($l_d \sim 27$ mm in our experiment) to $BFD \sim 17.8$ cm. In addition, the time-domain THz integration was again observed, as indicated in Figs. 4(f)–4(h), with $RMSE \sim 14\%$, well supporting our theory. Comparing Figs. 4(d) and 4(h), the polarities of these two THz electric fields were completely reversed, which was also induced by the change of BFD by a dephasing length, as expected in Ref. 42.

VI. TIME-DOMAIN THz INTEGRATION INSIDE THE FOUR-FILAMENT ARRAY

One advantage of the suggested all-optical computing stage is the rapid reversibility of the air plasma, which can be either built up within the same temporal scale of the pumping laser pulse duration (i.e., a few tens of femtoseconds) or erased in nanoseconds (i.e., the lifetime of plasma) as long as the driven laser is removed. If further taking the thermal effect induced by the high laser repetition frequency^{16–18} into account, the air restoration time is still very short, i.e., on a timescale of milliseconds. This performance could be much quicker than the relaxation time of the reported LGL materials

(e.g., gel¹¹). Therefore, theoretically, in our case, the reconfiguration of the system is only limited by the time-consuming nature of common experimental operations, e.g., moving the BBO crystal to proper positions (Sec. V) or changing the phase plate type (in this section). Furthermore, it can be seen in Fig. 4(e) that the minimum error for THz integration by double filaments (black bars) was about 15%, which might not be good enough. This result can be attributed to the fact that not all THz energy was confined inside the two filaments' gap, and a significant portion of it existed as the periphery THz mode along individual filaments, as shown in Fig. 1(h). Therefore, this problem could be resolved by creating more gaps with a multiple-filament structure and totally squeezing THz waves into gap areas, which has been realized as follows.

Here, the time-domain THz integration effect has been explored by using a parallel four-filament array, which was produced by a quarter-circle phase plate (QCPP).¹⁹ Similar procedures to the previous double-filament experiment were performed in this four-filament case. For example, this time, E_{in} was the average of $E_1, E_2, E_3,$ and E_4 , which were the THz pulses radiated from each of the four filaments by blocking one quarter of the phase plate. In addition, E_{out} was the THz signal from the whole filament array. The final data are shown in Fig. 5, from which one can see all the same characteristics aforementioned in Fig. 4, including (i) the considerable enhancement of the low-frequency components of E_{out} , (ii) the $1/f$ tendency of $\mathcal{F}[E_{out}]/\mathcal{F}[E_{in}]$ as shown in Figs. 5(a) and 5(c), (iii) the satisfying match between E_{in} and dE_{out}/dt , and (iv) the inverse symmetry of THz waveforms given by two BFDs separated by a dephasing length as shown in Figs. 5(b) and 5(d).

Compared with the double-filament array, this four-filament pattern has been a better time integrator, as expected. In addition, the calculated RMSE between E_{in} and dE_{out}/dt in Figs. 5(b) and 5(d) is only 8%. More information can be found in supplementary material S11. It is promising to further decrease the error value by

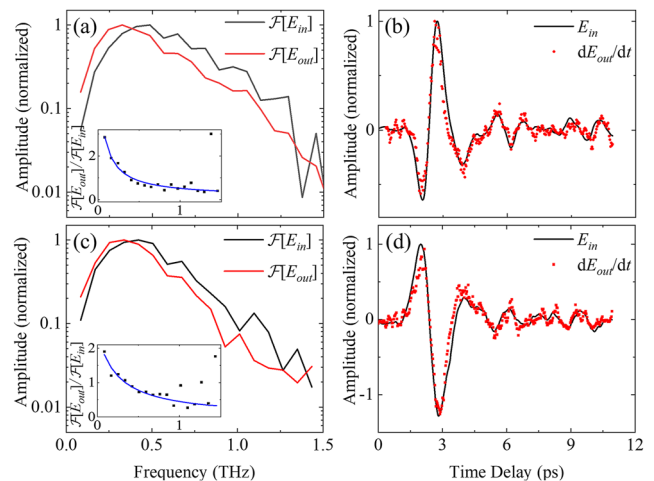


FIG. 5. For the four-filament arrays: (a) THz spectra of E_{in} ($\mathcal{F}[E_{in}]$, black line) and E_{out} ($\mathcal{F}[E_{out}]$, red line). Inset: $[E_{out}]/\mathcal{F}[E_{in}]$ (black squares) and its $1/f$ -fitted curve (blue line). (b) E_{in} (black line) and the first-order time derivative of E_{out} (i.e., dE_{out}/dt , red circles). (c) and (d) THz signals recorded in the case of the BBO crystal being moved toward the laser focus by a $\omega-2\omega$ dephasing length.

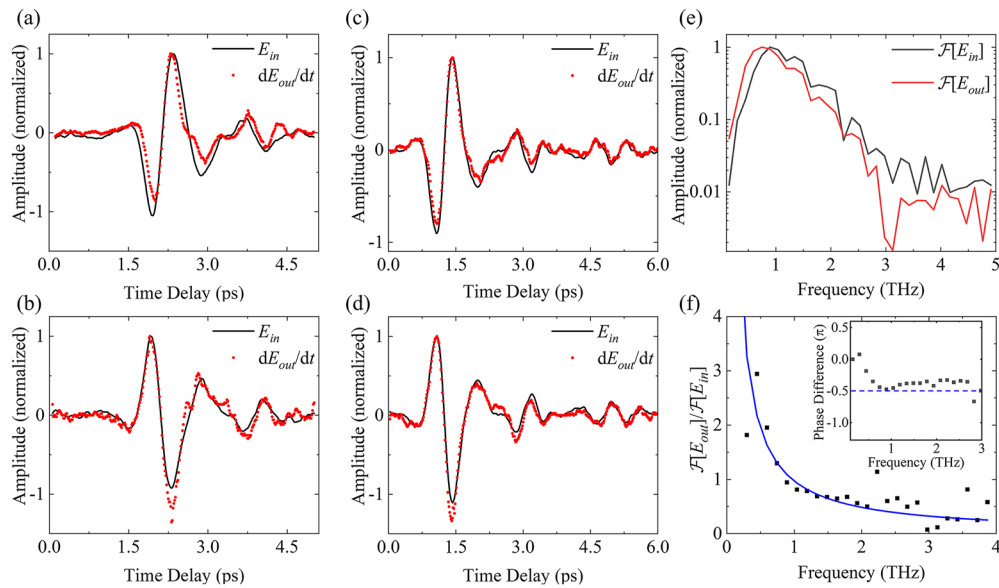


FIG. 6. In a broader THz bandwidth, experimental results of the double filaments (a) and (b) and the four filaments (c) and (d), and the spectral information (e) and (f) induced by the temporal integration effect based on (c).

optimizing the filament array's construction, e.g., the filament number, length, and structure, in order to achieve a stronger confinement of all THz power inside the ENZ gaps between each of the multiple filaments.

VII. ADDITIONAL EXPERIMENTS IN BROADER THz BANDWIDTH

We have replaced the original ZnTe crystal with a thinner one (0.5 mm), thereby increasing the spectral width to 3 THz, as shown in Fig. 6. Specifically, Figs. 6(a) and 6(b) depict the experimental results obtained with the double filaments, and Figs. 6(c) and 6(d) illustrate those obtained with the four filaments. The associated integration errors of these four figures are about 13%, 9%, 6%, and 5%, respectively. Figure 6(e) further represents the current spectral bandwidth achieved by us. In addition, Fig. 6(f) indicates the spectral amplitude and phase of the transfer function, as expected.

It is worth noting that, during the above experimental measurements, we slowed down the scanning speed of the delay line and increased the time constant of the lock-in amplifier. As a result, the acquired waveforms became more stable and smoother, and the differentiation results (dE_{out}/dt) did not exhibit as many fluctuations as those in Figs. 4 and 5. All these improvements have contributed to the reduction of integration errors.

VIII. DISCUSSION

The similarity between E_{in} and E_{out} , as shown in Fig. 4(b) or Fig. 4(f), might be misleading as if these two signals were actually the same with a relative time delay instead of an integration relationship. This issue can be clarified by manually overlapping E_{in} and E_{out} in the time domain (supplementary material S12). It can be seen that

the corresponding profile matching is far from what we proposed. Moreover, the spectral amplitudes of E_{in} and E_{out} show a clear $1/f$ connection, which cannot be resulted from a time delay between two identical THz pulses.

In addition, the suggested all-optical method can not only serve as a tabletop computing “chip” with a sub-millimeter-scale information channel but can also be applied during remotely directional transmission of THz waves in the air, e.g., cascaded with the free-space photonic crystal (FPC).²³ In this case, the unwanted weak THz differentiation effect of the FPC waveguide (supplementary material S13) could be counteracted by the following THz integration given by the double- or four-filament stage. Therefore, a THz signal far away after long-distance guided travel can be recovered to its original shape by remotely controlling the all-filament setup. If further mixed with the BFD-tuned superposition mode (in Sec. V) and the amplitude division pattern by crossing two filaments,³⁹ it is promising to realize an air-plasma-based all-optical hybrid computation station in free space.

It is also worth mentioning that, besides our laser-guiding-THz manner,^{15,36,39,43} the phenomena of LGL in air are also observed in other frequency bands, like laser-guiding-microwaves,^{44–51} infrared,^{52,53} visible light,^{54–60} and even x rays.⁶¹ Hence, the proposed method in this work is promising to serve as a prototype for extending all-optical calculations throughout the entire electromagnetic (EM) spectrum. Moreover, our air-based LGL THz computing could be potentially combined with THz wireless transmission, sensing, or communication,⁶² which would allow remote manipulation and directional processing of THz signals at any free-space location as long as air is available. Furthermore, considering the scalability of the frequency bands mentioned above, air-based all-optical computing and wireless applications can be theoretically beyond the THz range.

IX. CONCLUSION

In summary, in this work, we developed a non-static platform for LGL integration of broadband THz pulses based on the air plasma. Briefly, this all-optical stage was dynamically constructed by laser-ionization-induced transient plasma waveguide circuits in flexible conversion between two- and four-filament arrays due to the reversibility of air. Then, the THz signal was spatially confined along the ENZ area of the plasma structure, resulting in a spectral response in $1/f$ shape, which accounted for the final THz integration phenomenon. This atmospheric LGL scheme for optical signal processing has been realized merely by interactions between light beams without assistance from conventional solid waveguide circuits or devices, thus paving the way toward new approaches to all-optical computing without complex hardware and algorithms. In future developments, our prototype setup holds the potential to become a building block for the construction of a wide range of analog systems for THz signal transmission, processing, and computing applications.^{63–65}

SUPPLEMENTARY MATERIAL

See the supplementary material for additional information.

ACKNOWLEDGMENTS

This work was supported in part by National Natural Science Foundation of China (Grant No. 61988102, 62335012), Youth Sci-Tech “Qimingxing” (Grant No. 22QC1400300) Program of Shanghai, and National Key Research and Development Program (2022YFA1404004).

AUTHOR DECLARATIONS

Conflict of Interest

The authors have no conflicts to disclose.

Author Contributions

Jiayu Zhao: Conceptualization (lead); Methodology (equal); Writing – original draft (lead); Writing – review & editing (lead). **Feifan Zhu:** Software (equal); Writing – original draft (equal); Writing – review & editing (equal). **Yongpeng Han:** Software (equal); Writing – original draft (equal); Writing – review & editing (equal). **Qining Wang:** Investigation (equal); Software (equal); Writing – original draft (equal); Writing – review & editing (supporting). **Li Lao:** Resources (supporting); Writing – review & editing (equal). **Xiaofeng Li:** Investigation (equal); Writing – original draft (equal). **Yan Peng:** Resources (supporting); Writing – review & editing (equal). **Yiming Zhu:** Resources (supporting); Writing – review & editing (equal).

DATA AVAILABILITY

The data underlying the results presented in this paper are not publicly available at this time but may be obtained from the authors upon reasonable request.

REFERENCES

- M. Ferrera, Y. Park, L. Razzari, B. E. Little, S. T. Chu, R. Morandotti, D. J. Moss, and J. Azaña, “On-chip CMOS-compatible all-optical integrator,” *Nat. Commun.* **1**, 29 (2010).
- J. Feldmann, M. Stegmaier, N. Gruhler, C. Ríos, H. Bhaskaran, C. D. Wright, and W. H. P. Pernice, “Calculating with light using a chip-scale all-optical abacus,” *Nat. Commun.* **8**, 1256 (2017).
- G. Balistreri, A. Tomasino, J. Dong, A. Yurtsever, S. Stivala, J. Azaña, and R. Morandotti, “Time-domain integration of broadband terahertz pulses in a tapered two-wire waveguide,” *Laser Photonics Rev.* **15**, 2100051 (2021).
- J. L. Dong, A. Tomasino, G. Balistreri, P. You, A. Vorobiov, É. Charette, B. Le Drogoff, M. Chaker, A. Yurtsever, S. Stivala, M. A. Vincenti, C. De Angelis, D. Kip, J. Azaña, and R. Morandotti, “Versatile metal-wire waveguides for broadband terahertz signal processing and multiplexing,” *Nat. Commun.* **13**, 741 (2022).
- J. Azaa, “Ultrafast analog all-optical signal processors based on fiber-grating devices,” *IEEE Photonics J.* **2**, 359 (2010).
- A. Alù and N. Engheta, “All optical metamaterial circuit board at the nanoscale,” *Phys. Rev. Lett.* **103**, 143902 (2009).
- M. Miscuglio, Y. Gui, X. Ma, Z. Z. Ma, S. Sun, T. El Ghazawi, T. Itoh, A. Alù, and V. J. Sorger, “Approximate analog computing with metatronic circuits,” *Commun. Phys.* **4**, 196 (2021).
- J. Chang, V. Sitzmann, X. Dun, W. Heidrich, and G. Wetzstein, “Hybrid optical-electronic convolutional neural networks with optimized diffractive optics for image classification,” *Sci. Rep.* **8**, 12324 (2018).
- Y. Luo, D. Mengü, N. T. Yardimci, Y. Rivenson, M. Veli, M. Jarrahi, and A. Ozcan, “Design of task-specific optical systems using broadband diffractive neural networks,” *Light Sci. Appl.* **8**, 112 (2019).
- M. Miscuglio, Z. Hu, S. Li, J. K. George, R. Capanna, H. Dalir, P. M. Bardet, P. Gupta, and V. J. Sorger, “Massively parallel amplitude-only Fourier neural network,” *Optica* **7**, 1812 (2020).
- D. R. Morim, A. Meeks, A. Shastri, A. Tran, A. V. Shneidman, V. V. Yashin, F. Mahmood, A. C. Balazs, J. Aizenberg, and K. Saravanamuttu, “Opto-chemomechanical transduction in photoresponsive gels elicits switchable self-trapped beams with remote interactions,” *Proc. Natl. Acad. Sci. U. S. A.* **117**, 3953 (2020).
- A. D. Hudson, M. R. Ponte, F. Mahmood, T. Pena Ventura, and K. Saravanamuttu, “A soft photopolymer cuboid that computes with binary strings of white light,” *Nat. Commun.* **10**, 2310 (2019).
- S. L. Chin, S. A. Hosseini, W. Liu, Q. Luo, F. Théberge, N. Aközbeke, A. Becker, V. P. Kandidov, O. G. Kosareva, and H. Schroeder, “The propagation of powerful femtosecond laser pulses in optical media: Physics, applications, and new challenges,” *Can. J. Phys.* **83**, 863 (2005).
- A. Couairon and A. Mysyrowicz, “Femtosecond filamentation in transparent media,” *Phys. Rep.* **441**, 47 (2007).
- J. Y. Zhao, W. Chu, Z. Wang, Y. Peng, C. Gong, L. Lin, Y. M. Zhu, W. W. Liu, Y. Cheng, S. L. Zhuang, and Z. Z. Xu, “Strong spatial confinement of terahertz wave inside femtosecond laser filament,” *ACS Photonics* **3**, 2338 (2016).
- Y. H. Cheng, J. K. Wahlstrand, N. Hajji, and H. M. Milchberg, “The effect of long timescale gas dynamics on femtosecond filamentation,” *Opt. Express* **21**, 4740 (2013).
- P. Walch, B. Mahieu, L. Arantchouk, Y. B. André, A. Mysyrowicz, and A. Houard, “Cumulative air density depletion during high repetition rate filamentation of femtosecond laser pulses: Application to electric discharge triggering,” *Appl. Phys. Lett.* **119**, 264101 (2021).
- A. D. Koulouklidis, C. Lanara, C. Daskalaki, V. Y. Fedorov, and S. Tzortzakos, “Impact of gas dynamics on laser filamentation THz sources at high repetition rates,” *Opt. Lett.* **45**, 6835 (2020).
- H. Gao, W. Chu, G. L. Yu, B. Zeng, J. Y. Zhao, Z. Wang, W. W. Liu, Y. Cheng, and Z. Z. Xu, “Femtosecond laser filament array generated with step phase plate in air,” *Opt. Express* **21**, 4612 (2013).
- H. Gao, J.-Y. Zhao, and W.-W. Liu, “Control of multiple filamentation induced by ultrafast laser pulses,” *Opt. Precis. Eng.* **21**, 598 (2013).
- N. A. Panov, O. G. Kosareva, and I. N. Murtazin, “Ordered filaments of a femtosecond pulse in the volume of a transparent medium,” *J. Opt. Technol.* **73**, 778 (2006).

- ²²J. Y. Zhao *et al.*, “Observation of the epsilon-near-zero (ENZ) effect inside the laser plasma in air,” *arXiv:2211.06796* (2022).
- ²³L. Z. Tang, J. Y. Zhao, Z. H. Dong, Z. H. Liu, W. T. Xiong, Y. C. Hui, A. Shkurinov, Y. Peng, and Y. M. Zhu, “Towards remotely directional transmission of terahertz wave in air: The concept of free-space photonic crystal waveguide,” *Opt Laser Technol.* **141**, 107102 (2021).
- ²⁴K. L. Wang, D. Mittleman, N. C. J. van der Valk, and P. Planken, “Antenna effects in terahertz apertureless near-field optical microscopy,” *Appl. Phys. Lett.* **85**, 2715 (2004).
- ²⁵M. A. Seo, H. R. Park, S. M. Koo, D. J. Park, J. H. Kang, O. K. Suwal, S. S. Choi, P. C. M. Planken, G. S. Park, N. K. Park, Q. H. Park, and D. S. Kim, “Terahertz field enhancement by a metallic nano slit operating beyond the skin-depth limit,” *Nat. Photonics* **3**, 152 (2009).
- ²⁶A. Alú and N. Engheta, “Light squeezing through arbitrarily shaped plasmonic channels and sharp bends,” *Phys. Rev. B* **78**, 035440 (2008).
- ²⁷M. G. Silveirinha and N. Engheta, “Theory of supercoupling, squeezing wave energy, and field confinement in narrow channels and tight bends using ϵ near-zero metamaterials,” *Phys. Rev. B* **76**, 245109 (2007).
- ²⁸J. Y. Zhao, Q. N. Wang, Y. C. Hui, Y. Chen, F. Zhu, Z. Jin, A. P. Shkurinov, Y. Peng, Y. Zhu, S. Zhuang, and L. Lao, “Traveling-wave antenna model for terahertz radiation from laser-plasma interactions,” *SciPost Phys. Core* **5**, 046 (2022).
- ²⁹J. Gosciniaik, Z. B. Hu, M. Thomaschewski, V. J. Sorger, and J. B. Khurgin, “Bistable all-optical devices based on nonlinear epsilon-near-zero (ENZ) materials,” *Laser Photonics Rev.* **17**, 2200723 (2023).
- ³⁰R. Amin, J. K. George, S. Sun, T. Ferreira de Lima, A. N. Tait, J. B. Khurgin, M. Miscuglio, B. J. Shastri, P. R. Prucnal, T. El-Ghazawi, and V. J. Sorger, “ITO-based electro-absorption modulator for photonic neural activation function,” *APL Mater.* **7**, 081112 (2019).
- ³¹H. Li, P. Y. Fu, Z. Z. Zhou, W. Y. Sun, Y. Li, J. M. Wu, and Q. H. Dai, “Performing calculus with epsilon-near-zero metamaterials,” *Sci. Adv.* **8**, eabq6198 (2022).
- ³²H. G. Roskos, M. D. Thomson, M. Krieb, and T. Löffler, “Broadband THz emission from gas plasmas induced by femtosecond optical pulses: From fundamentals to applications,” *Laser Photonics Rev.* **1**, 349 (2007).
- ³³M. Durand, Y. Liu, A. Houard, and A. Mysyrowicz, “Fine control of terahertz radiation from filamentation by molecular lensing in air,” *Opt. Lett.* **35**, 1710 (2010).
- ³⁴Q. Y. Song, X. M. Yuan, S. S. Hu, J. F. Huang, H. Z. Zhong, Q. G. Lin, H. G. Wang, X. W. Lu, M. J. Zheng, Y. Cai, X. K. Zeng, and S. X. Xu, “Enhance terahertz radiation and its polarization-control with two parallel filaments pumped by two-color femtosecond laser fields,” *Opt. Express* **29**, 22659 (2021).
- ³⁵K. Y. Kim, J. H. Glowina, A. J. Taylor, and G. Rodriguez, “Terahertz emission from ultrafast ionizing air in symmetry-broken laser fields,” *Opt. Express* **15**, 4577 (2007).
- ³⁶J. Y. Zhao, W. W. Liu, S. C. Li, D. Lu, Y. Z. Zhang, Y. Peng, Y. M. Zhu, and S. L. Zhuang, “Clue to a thorough understanding of terahertz pulse generation by femtosecond laser filamentation,” *Photonics Res.* **6**, 296 (2018).
- ³⁷Z. Q. Yu, N. Zhang, J. X. Wang, Z. J. Dai, C. Gong, L. Lin, L. J. Guo, and W. Liu, “0.35% THz pulse conversion efficiency achieved by Tisapphire femtosecond laser filamentation in argon at 1 kHz repetition rate,” *Opto-Electron. Adv.* **5**, 210065 (2022).
- ³⁸E. Cabrera-Granado, Y. X. Chen, I. Babushkin, L. Bergé, and S. Skupin, “Spectral self-action of THz emission from ionizing two-color laser pulses in gases,” *New J. Phys.* **17**, 023060 (2015).
- ³⁹H. W. Du, H. Hoshina, C. Otani, and K. Midorikawa, “Terahertz waves radiated from two noncollinear femtosecond plasma filaments,” *Appl. Phys. Lett.* **107**, 211113 (2015).
- ⁴⁰J. Y. Zhao, L. J. Guo, W. Chu, B. Zeng, H. Gao, Y. Cheng, and W. W. Liu, “Simple method to enhance terahertz radiation from femtosecond laser filament array with a step phase plate,” *Opt. Lett.* **40**, 3838 (2015).
- ⁴¹Y. S. You, T. I. Oh, and K. Y. Kim, “Off-axis phase-matched terahertz emission from two-color laser-induced plasma filaments,” *Phys. Rev. Lett.* **109**, 183902 (2012).
- ⁴²K. Y. Kim, A. J. Taylor, J. H. Glowina, and G. Rodriguez, “Coherent control of terahertz supercontinuum generation in ultrafast laser-gas interactions,” *Nat. Photonics* **2**, 605 (2008).
- ⁴³J. Y. Zhao, W. Chu, L. J. Guo, Z. Wang, J. Yang, W. W. Liu, Y. Cheng, and Z. Z. Xu, “Terahertz imaging with sub-wavelength resolution by femtosecond laser filament in air,” *Sci. Rep.* **4**, 3880 (2014).
- ⁴⁴M. Alshershby, Y. Ren, J. Qin, Z. Q. Hao, and J. Q. Lin, “Diagnosis of femtosecond plasma filament by channeling microwaves along the filament,” *Appl. Phys. Lett.* **102**, 204101 (2013).
- ⁴⁵M. Alshershby, Z. Q. Hao, and J. Q. Lin, “Analysis of microwave leaky modes propagating through laser plasma filaments column waveguide,” *Phys. Plasmas* **19**, 123504 (2012).
- ⁴⁶M. Alshershby, Z. Q. Hao, and J. Q. Lin, “Guiding microwave radiation using laser-induced filaments: The hollow conducting waveguide concept,” *J. Phys. D: Appl. Phys.* **45**, 265401 (2012).
- ⁴⁷V. D. Zvorykin, A. O. Levchenko, A. V. Shutov, E. V. Solomina, N. N. Ustinovskii, and I. V. Smetanin, “Long-distance directed transfer of microwaves in tubular sliding-mode plasma waveguides produced by KrF laser in atmospheric air,” *Phys. Plasmas* **19**, 033509 (2012).
- ⁴⁸Y. Ren, M. Alshershby, Z. Q. Hao, Z. M. Zhao, and J. Q. Lin, “Microwave guiding along double femtosecond filaments in air,” *Phys. Rev. E* **88**, 013104 (2013).
- ⁴⁹Y. Ren, M. Alshershby, J. Qin, Z. Q. Hao, and J. Q. Lin, “Microwave guiding in air along single femtosecond laser filament,” *J. Appl. Phys.* **113**, 094904 (2013).
- ⁵⁰M. Châteauneuf, S. Payeur, J. Dubois, and J. C. Kieffer, “Microwave guiding in air by a cylindrical filament array waveguide,” *Appl. Phys. Lett.* **92**, 091104 (2008).
- ⁵¹V. V. Valuev, A. E. Dormidonov, V. P. Kandidov, S. A. Shlenov, V. N. Kornienko, and V. A. Cherepenin, “Plasma channels formed by a set of filaments as a guiding system for microwave radiation,” *J. Commun. Technol. Electron.* **55**, 208 (2010).
- ⁵²M. Alshershby, Z. Q. Hao, A. Camino, and J. Q. Lin, “Modeling a femtosecond filament array waveguide for guiding pulsed infrared laser radiation,” *Opt. Commun.* **296**, 87 (2013).
- ⁵³C. G. Durfee and H. M. Milchberg, “Light pipe for high intensity laser pulses,” *Phys. Rev. Lett.* **71**, 2409 (1993).
- ⁵⁴B. Miao, L. Feder, J. E. Shrock, A. Goffin, and H. M. Milchberg, “Optical guiding in meter-scale plasma waveguides,” *Phys. Rev. Lett.* **125**, 074801 (2020).
- ⁵⁵L. Feder, B. Miao, J. E. Shrock, A. Goffin, and H. M. Milchberg, “Self-waveguiding of relativistic laser pulses in neutral gas channels,” *Phys. Rev. Res.* **2**, 043173 (2020).
- ⁵⁶E. W. Rosenthal, N. Jhaji, J. K. Wahlstrand, and H. M. Milchberg, “Collection of remote optical signals by air waveguides,” *Optica* **39**, 6312 (2014).
- ⁵⁷A. Goffin, A. Tartaro, and H. M. Milchberg, “Quasi-steady-state air waveguide,” *Optica* **10**, 505 (2023).
- ⁵⁸Y. Cheng, “Air waveguide from ‘donut’ laser beams,” *Physics* **16**, 11 (2023).
- ⁵⁹N. Jhaji, E. W. Rosenthal, R. Birnbaum, J. K. Wahlstrand, and H. M. Milchberg, “Demonstration of long-lived high-power optical waveguides in air,” *Phys. Rev. X* **4**, 011027 (2014).
- ⁶⁰A. Goffin, I. Larkin, A. Tartaro, A. Schweinsberg, A. Valenzuela, E. W. Rosenthal, and H. M. Milchberg, “Optical guiding in 50-meter-scale air waveguides,” *Phys. Rev. X* **13**, 011006 (2023).
- ⁶¹H. M. Milchberg, T. R. Clark, C. G. Durfee, T. M. Antonsen, and P. Mora, “Development and applications of a plasma waveguide for intense laser pulses,” *Phys. Plasmas* **3**, 2149 (1996).
- ⁶²J. M. Jornet, E. W. Knightly, and D. M. Mittleman, “Wireless communications sensing and security above 100 GHz,” *Nat. Commun.* **14**, 841 (2023).
- ⁶³Y. Peng, J. L. Huang, J. Luo, Z. F. Yang, L. P. Wang, X. Wu, X. F. Zang, C. Yu, M. Gu, Q. Hu, X. C. Zhang, Y. M. Zhu, and S. L. Zhuang, “Three-step one-way method in terahertz biomedical detection,” *PhotonIX* **2**, 12 (2021).
- ⁶⁴Y. Zhu, X. F. Zang, H. X. Chi, Y. W. Zhou, Y. M. Zhu, and S. L. Zhuang, “Metasurfaces designed by a bidirectional deep neural network and iterative algorithm for generating quantitative field distributions,” *Light: Adv. Manuf.* **4**, 9 (2023).
- ⁶⁵X. Z. Zang, B. S. Yao, L. Chen, J. Y. Xie, X. G. Guo, A. V. Balakin, A. P. Shkurinov, and S. L. Zhuang, “Metasurfaces for manipulating terahertz waves,” *Light: Adv. Manuf.* **2**, 10 (2021).